J. Fluid Mech. (2019), *vol.* 880, *pp.* 594–619.
doi:10.1017/jfm.2019.729

Steepened Mach waves near supersonic jets: study of azimuthal structure and generation process using conditional averages

Pierre Pineau[1],† **and Christophe Bogey**[1]

[1]Univ Lyon, École Centrale de Lyon, INSA Lyon, Université Claude Bernard Lyon I, CNRS, Laboratoire de Mécanique des Fluides et d'Acoustique, UMR 5509, F-69134 Ecully, France

(Received 21 December 2018; revised 27 August 2019; accepted 30 August 2019)

The azimuthal structure and the generation process of steepened acoustic waves are investigated in the near field of temporal round jets at Mach numbers of 2 and 3. Initially, the shear layers of the jets are in a laminar state and display instability waves whose main properties are close to those predicted from linear temporal analysis. Then, they transition to a turbulent state and generate high-intensity Mach waves displaying sharp compressions typical of those recorded for jets producing crackle noise. These waves are first shown to be poorly reproduced when only the axisymmetric mode is considered, but to be well captured with the first five azimuthal modes. Their generation process is investigated by performing conditional averages of the flow and acoustic fields triggered by the detection of intense positive pressure peak close to the jets. No steepened waves are visible in the conditionally averaged pressure profiles when the procedure involves only one azimuthal mode at a time. However, sharp compressions are obtained based on the first five modes taken together. In that case, the steep compressions are correlated over a limited portion of the jet circumference and are steeper as more azimuthal modes are considered. Moreover, a direct link is established between the steepened waves and the supersonic convection of large-scale coherent flow structures located in the supersonic core of the jets. This indicates that these waves constitute an extreme, nonlinear case of Mach wave radiation by these structures. In addition, the capacity of flow structures to generate sharp, steepened waves is related to their shapes. More particularly, flow structures with a large extent in the radial direction are shown to produce stronger and steeper Mach waves than those that are elongated in the flow direction.

Key words: aeroacoustics, jet noise

1. Introduction

It is now well recognised that the noise generated by highly supersonic jets at low outlet angles is related to the motion of large-scale coherent structures inside the flow (McLaughlin, Morisson & Troutt 1975; Troutt & McLaughlin 1982; Tam, Chen & Seiner 1992). When the convection velocity of these structures exceeds

† Email address for correspondence: pierre.pineau@doctorant.ec-lyon.fr

the ambient speed of sound, they generate Mach waves which propagate in the far field, leading to a peak of sound emission in the direction of the Mach angle as observed, for instance, by Seiner *et al.* (1992). A distinctive feature of the sound waves radiated in this direction is the presence of steep, jagged shock structures in the far acoustic field (Ffowcs Williams, Simson & Virchis 1975; Laufer, Schlinker & Kaplan 1976; Krothapalli, Venkatakrishnan & Lourenco 2000; Baars & Tinney 2014). These steepened waves are believed to be the cause of crackle, an unpleasant perception effect first described by Ffowcs Williams *et al.* (1975). Despite several years of research, the mechanisms leading to their formation remain unclear. Notably, an important issue is to distinguish the respective roles of propagation and source effects in their formation process. It is well known that the pressure levels generated by highly supersonic jets are so high that nonlinear propagation effects must be taken into account to accurately describe the propagation of sound. The accumulation of these phenomena induces a gradual steepening of the wavefronts leading to the formation of shocks (Crighton & Bashforth 1980; Morfey & Howell 1980; Enflo & Hedberg 2002). For instance, in their simulation of the noise generated by a Mach 3.3 hot jet, de Cacqueray & Bogey (2014) pointed out the progressive formation of N-shaped waves resulting from a nonlinear energy transfer from middle to high frequencies. Similar observations have also been made in the sound field of full-scale jet engines, as shown by Gee *et al.* (2007) or Reichman *et al.* (2017), for instance. However, nonlinear propagation effects are less prevailing in the case of experiments conducted at the laboratory scale (Gallagher & McLaughlin 1981; Petitjean & McLaughlin 2003; Petitjean, Viswanathan & McLaughlin 2006; Baars, Tinney & Hamilton 2014). In such experiments, the peak frequencies are higher and molecular absorption, which can counteract the formation of shocks, is thus significant. By taking into account the role of molecular absorption, Baars *et al.* (2014) and Baars, Tinney & Hamilton (2016) predicted that nonlinear steepening, alone, could not account for the presence of shocks in the sound field of their small-scale laboratory jet. Therefore, there must be some other mechanism at play. Optical visualisations of the near acoustic field radiated by very high-speed jets and mixing layers (Lowson & Ollerhead 1968; Papamoschou 1995; Rossmann, Mungal & Hanson 2001) have shown the presence of shocks, whose tips appear to be embedded inside the turbulent flow. As sketched in Rossmann *et al.* (2001), the formation of these waves is expected to be linked to the supersonic motion of flow structures, acting as bluff bodies or wavy walls, and yielding to the formation of shocklets in the interfacial region between the turbulent flow and the ambient medium. In their simulation of plane temporally developing mixing layers, Buchta & Freund (2017) observed the formation of such shocklets in the immediate vicinity of the shear layers. As these shocks propagate away from the flow, they merge with each other, resulting in fewer but stronger and steeper waves with increasing propagation distance. This shock coalescence mechanism has also been observed experimentally in the near acoustic field of a Mach 3 jet by Fiévet *et al.* (2016) and is expected to play a key role in the formation of crackle. All of these observations strongly suggest that shock formation can also occur at the source, in and near the jet flow. However, the precise mechanisms involved are currently not well understood.

In order to clarify this point, Nichols *et al.* (2013*a*), Nichols, Lele & Spyropoulos (2013*b*) performed large eddy simulations (LES) of hot supersonic jets. They observed that strong Mach waves of very steep nature are intermittently generated from the shear layers of the jets and can be attributed to the occurrence of violent events inside the jets. Murray & Lyons (2016) measured the propagation angles of the shocks

generated in the near field of a hot Mach 1.55 jet. Assuming these shocks are Mach waves, they investigated the statistical distribution of the resulting convection velocities and found that they follow an extreme value distribution. These studies suggest that crackle events can be comprehended as extreme, nonlinear occurrences of Mach wave radiation. The mechanism by which Mach waves are generated has received a lot of attention in the last decades (Tam & Morris 1980; Tam & Burton 1984*a*,*b*; Tam *et al.* 1992) and is now reasonably well understood. A simplified view originally proposed by Ribner (1969) is that the velocity disturbances induced by a train of coherent structures can be seen as a travelling wavy wall along which the flow is successively compressed and expanded. When the convection velocity of the structures is supersonic, the pressure perturbations resulting from these compression–expansion processes propagate in the far field as sound. While this model provides a direct and simple explanation of the Mach wave phenomenon, any further attempt to explain how shocks can be formed as a result of this mechanism requires additional information on the nature and the dynamics of coherent structures in high-speed jets. At the present time, this can be very challenging since the very concept of a coherent structure is not even clearly defined (Hussain 1983; Jordan & Colonius 2013). In order to bridge that gap, several researchers have tried to model coherent structures as linear instability waves (Tam & Burton 1984*a*,*b*; Tam *et al.* 1992; Sinha *et al.* 2014). While this approach has been successful in predicting several aspects of Mach wave radiation, such as the convection velocity of the structures, the direction of peak sound emission or the shapes of far field spectra near the peak frequency (Tam & Burton 1984*b*; Tam *et al.* 1992; Mohseni & Colonius 2002; Sinha *et al.* 2014), its linear character does not allow us to take into account the possible formation of shocks. Consequently, there is a need for a deeper understanding of the generation process of Mach waves, as it could lead to a better understanding of the way shocks can be formed as a nonlinear by-product of this mechanism, and thus pave the way for future noise reduction strategies.

In the present study, the connection between the formation of steepened waves and the motion of large-scale coherent structures in supersonic jets is investigated by performing large eddy simulations of temporally developing round jets. These temporal simulations are used as simplified models of spatially developing jets, as in previous studies of sound generation in subsonic (Kleinman & Freund 2008; Bogey 2019) and supersonic free-shear flows (Buchta & Freund 2017). The jets considered are isothermal and have Mach numbers of 2 and 3, in order to explore the effects of this parameter on the properties of the flow structures which produce steepened waves. Indeed, the influence of the Mach number on the formation of these waves is known to be strong (Ffowcs Williams *et al.* 1975; Buchta & Freund 2017) but the means by which it influences noise generation and, in particular, the way it affects the large-scale flow structures are less obvious. In axisymmetric supersonic jets, large-scale coherent structures and the Mach waves that they generate are associated with low-order azimuthal modes of the pressure field, typically of order lower than two (Troutt & McLaughlin 1982; de Cacqueray, Bogey & Bailly 2011). Consequently, this raises the question of whether the sharp, shock-like compressions observed close to the jets also exhibit such a strong azimuthal correlation. In order to answer that question, one possibility is to examine whether steepened waves are present in low-order azimuthal modes of the near pressure field and, if so, to find out how many modes are necessary to recover those sharp compressions. In this way, the large-scale flow structures that generate steepened Mach waves could be extracted from these low-order modes and investigated separately with the aim to isolate the

particular mechanisms leading to the steepening of Mach waves. To achieve this, conditional averages triggered by positive pressure peaks in the jet near field provide a useful tool, since they allow to highlight the most generic features of flow events associated with intense sound generation (Pineau & Bogey 2018; Schmidt & Schmid 2019). They are thus applied to the present simulation results in order to provide some information on the flow structures correlated with the waves.

The paper is organised as follows: the main characteristics and numerical parameters of the simulations are introduced in § 2, along with the results of a linear stability analysis conducted from the jet initial profiles. The simulation results, including snapshots of the flow development, wavenumber spectra and conditional averages are presented in § 3, and concluding remarks are given in § 4. Finally, the effects of the initial conditions on the development of instability waves are presented in appendix A and the convergence of the conditional averages is assessed in appendix B.

2. Simulations of temporally developing supersonic jets

2.1. *Jet parameters*

Two simulations of temporally developing isothermal round jets at Mach numbers $M_j = u_j/a_j$ of 2 and 3 are performed, where u_j is the initial centreline axial velocity and a_j is the speed of sound in the jet. The diameter-based Reynolds numbers $Re_D = u_j D/\nu$ of the jets is equal to 12 500, where $D = 2r_0$ is the jet initial diameter and ν the kinematic viscosity. The static temperature T_j in the jet core is equal to the ambient temperature T_∞ whose value is set to 293 K, and the ambient pressure is equal to 10^5 Pa. At $t = 0$, the simulations are initialised with a hyperbolic-tangent velocity profile whose shear-layer momentum thickness δ_θ is equal to $\delta_\theta/r_0 = 2/\sqrt{Re_D} = 0.018 r_0$, following an empirical law obtained for initially laminar subsonic jets (Zaman 1985). In order to trigger the transition of the jet shear layers from a laminar to a turbulent state, small perturbations are added at the initial time. These perturbations are solenoidal Gaussian ring vortices of radius r_0, whose half-widths are equal to $2\delta_\theta$, as proposed by Bogey, Bailly & Juvé (2003) in a simulation of a spatially developing subsonic jet. As in Bogey (2019), in the case of temporally developing subsonic jets, these vortices have random azimuthal phases and amplitudes and they are evenly spaced every Δz in the axial direction, where $\Delta z = 0.025 r_0$ is the axial mesh spacing. Their amplitudes are chosen so that the initial perturbation levels are $0.02 u_j$, so that the jet shear layers are initially in a weakly disturbed state.

The choice to consider simulations of temporal jets is motivated by the simplicity of these model flows in comparison with more realistic, spatially developing jets. Indeed, there is no effect of the nozzle in temporally developing jets, which makes the control of the initial development of the shear layers easier. Furthermore, the turbulent structures developing in these flows have length scales that are statistically uniform in the axial direction, which allows us to achieve high spatial resolutions at a relatively low computational cost. This simplicity comes at the price that no far acoustic field can be defined for temporally developing jets since they have two homogeneous directions. This could be a concern for the study of the steepening induced by nonlinear propagation effects or the wave merging process, as these phenomena occur over relatively long propagation distances and are thus affected by the spatial spreading of the jet. However, the present study focuses on the mechanisms responsible for the formation of steepened waves directly inside the turbulent flow. These mechanisms take place over very short length scales, typically of the order of the shear-layer thickness (Buchta & Freund 2019), hence are not expected to depend on the temporal or spatial nature of the flow.

2.2. *Numerical parameters*

The flow and sound fields of the temporal jets are computed using a numerical solver very similar to those used in previous simulations of spatially developing supersonic jets (de Cacqueray *et al.* 2011; Gojon & Bogey 2017). The unsteady compressible Navier–Stokes equations are solved in cylindrical coordinates using high-order finite differences. The spatial derivatives are computed using low-dispersion eleven-point centred finite difference schemes (Bogey & Bailly 2004; Berland *et al.* 2007), and an explicit six-stage Runge–Kutta method is used for time integration. At the end of each time step, grid-to-grid oscillations are removed by the application of a twelfth-order centred selective filter. In the simulations, which are very well resolved LES, the selective filter also acts as a subgrid-scale model that allows the relaxation of turbulent kinetic energy near the grid cutoff wavenumber (Bogey & Bailly 2006). In order to treat the axis singularity arising from the use of cylindrical coordinates, the method of Mohseni & Colonius (2002) is implemented. The discretisation point closest to the axis is located at $r = \Delta r/2$, where Δr is the radial mesh spacing near the axis. Moreover, the azimuthal derivatives near the jet centreline are computed using fewer points than permitted by the grid to alleviate the time-step restriction, as proposed in Bogey, Marsden & Bailly (2011). As a result, the effective azimuthal resolution progressively varies from 16 for the point nearest to the jet axis to 256 for $r \geqslant 0.25r_0$. The radiation boundary conditions of Tam & Dong (1996) are prescribed at the radial boundary to allow the acoustic waves to leave the computational domain without causing significant spurious reflections. Periodicity conditions are also imposed at the axial boundaries. Since the velocities of the jets are much higher than the speed of sound, shocks are expected in the simulations, which will lead to the formation of spurious Gibbs oscillations. In preliminary computations, it was found that these oscillations are weak for the Mach 2 jet but strong for the Mach 3 jet. For the latter case, Gibbs oscillations are thus damped by the application of a shock-capturing filtering (Bogey, de Cacqueray & Bailly 2009) at the end of each time step.

2.3. *Computational parameters*

The simulations are carried out using a cylindrical mesh extending up to $z = 240r_0$ in the axial direction and out to $r = 13r_0$ in the radial direction. The number of points in the radial, azimuthal and axial directions are respectively $n_r = 382$, $n_\theta = 256$ and $n_z = 9600$, yielding a total number of 940 million points. The axial mesh spacing is constant and equal to $\Delta z = 0.025r_0$, allowing an accurate resolution up to a wavenumber of $k_z r_0 = 62.8$, corresponding to a wavelength discretised by 4 points (Bogey & Bailly 2004). The radial mesh spacing Δr varies with the radial position. It is equal to $\Delta r = \Delta z$ on the jet axis and reaches a minimum value of $\Delta r_{min} = \Delta z/4$ at $r = r_0$. Then, it rises until it is equal to $0.05r_0$ for $r \geqslant 4r_0$. The simulations are performed using the OpenMP-based in-house solver developed by Bogey (2019) for subsonic temporal jets. The final simulation time is equal to $70r_0/u_j$ for the jet at $M_j = 2$ and to $120r_0/u_j$ for the jet at $M_j = 3$, which necessitated 8000 and 20 000 iterations, respectively. Finally, several runs of the same jets are performed using different initial perturbations of the shear layers by modifying the random seed used in the excitation procedure. This allows us to improve the convergence of the spatial statistics by ensemble averaging the results over all simulated runs. More particularly, the results obtained for the Mach 2 jets are computed over four runs whereas those for the Mach 3 jets are computed over three runs.

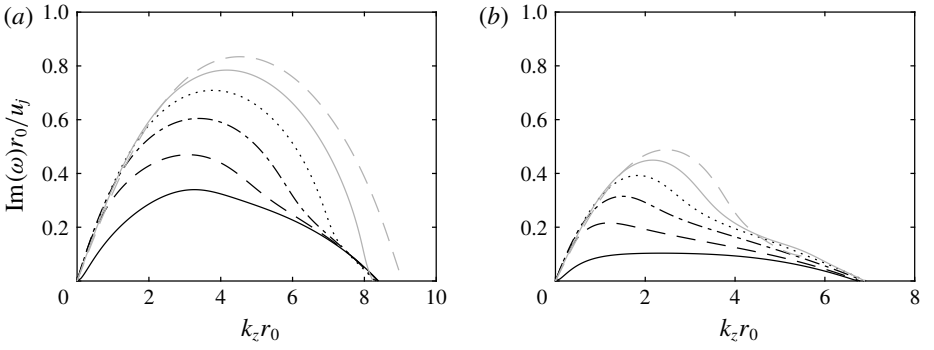

FIGURE 1. Amplification rates of the Kelvin–Helmholtz instability waves at $t = 0$ for (*a*) $M_j = 2$ and (*b*) $M_j = 3$; modes —— $n = 0$, - - - - $n = 1$, — · — $n = 2$, · · · · · · $n = 3$, —— (grey) $n = 4$ and - - - - (grey) $n = 5$.

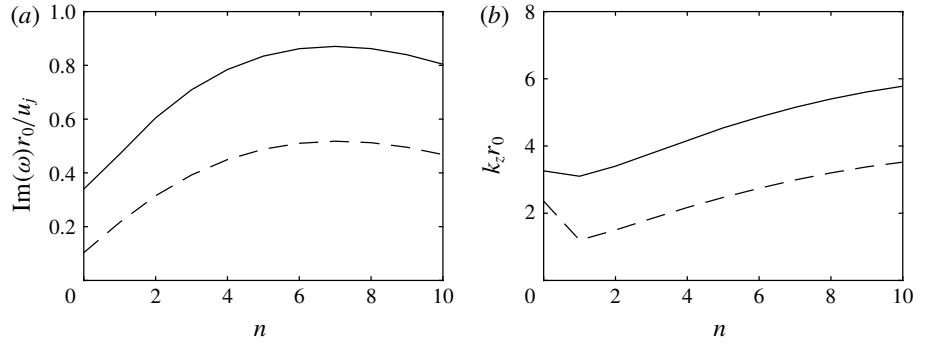

FIGURE 2. Representation of the (*a*) maximum amplification rate and (*b*) the most amplified axial wavenumber as a function of the azimuthal mode number for —— $M_j = 2$ and - - - - $M_j = 3$.

2.4. *Temporal stability analysis*

An inviscid temporal stability analysis is carried out from the initial velocity and density profiles. For a given axial wavenumber k_z and azimuthal mode n, the compressible Rayleigh equation is solved in cylindrical coordinates using a shooting method. This method combines the Euler method for the integration step and the secant method for the search of the complex angular frequency ω. The integration in the radial direction is performed on an homogeneous grid with a spacing of $0.0001r_0$, extending from the LES point closest to the jet axis out to $r = 5r_0$.

The amplification rates of the Kelvin–Helmholtz instability waves obtained for the first five azimuthal modes are represented in figure 1 as a function of the axial wavenumber for the two jets. For each azimuthal mode, they are positive over a broad range of axial wavenumbers, and reach maximum values over $3 \leqslant k_z r_0 \leqslant 5$ at Mach 2 and over $2 \leqslant k_z r_0 \leqslant 3$ at Mach 3. The peak amplification rates and their corresponding axial wavenumbers are plotted in figure 2 as a function of the mode number. For the two jets, the most amplified mode is mode $n = 7$. For this mode, the maximum amplification rate is obtained for $k_z r_0 = 5.2$ at Mach 2, and for $k_z r_0 = 3$ at Mach 3, yielding wavelengths of $1.2r_0$ and $2.1r_0$, respectively. Furthermore, for all azimuthal

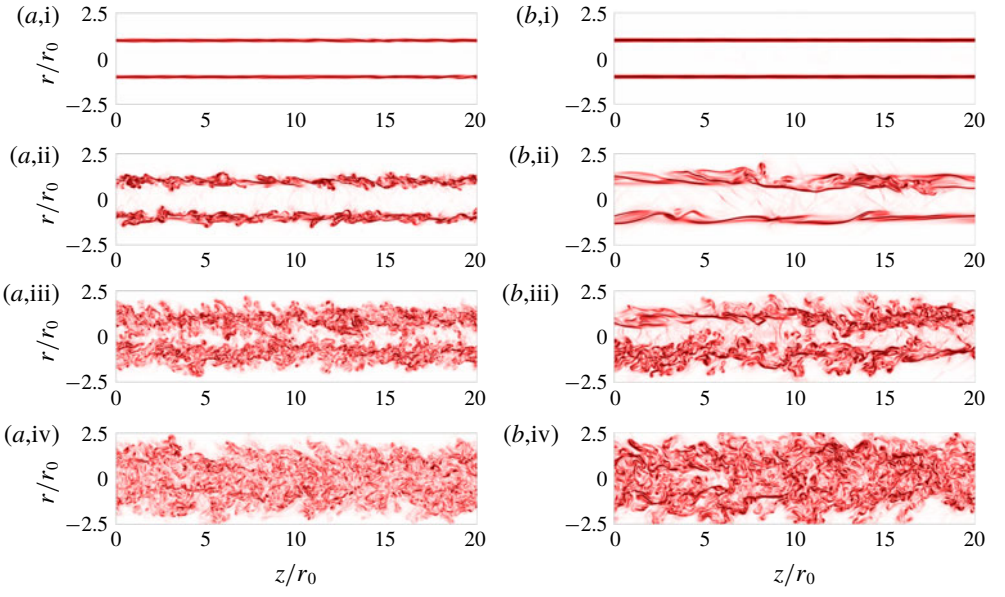

FIGURE 3. (Colour online) Vorticity norm for (*a*) $M_j = 2$ and (*b*) $M_j = 3$ at times (i) $t = 5r_0/u_j$, (ii) $t_c - 10r_0/u_j$, (iii) t_c and (iv) $t_c + 10r_0/u_j$. The colour scale ranges from 0 to $5u_j/r_0$, from white to red.

mode numbers, the maximum amplification rate is lower, and is reached for lower values of the axial wavenumber at Mach 2 than at Mach 3. This well-known effect of compressibility on the Kelvin–Helmholtz instability waves is expected to cause the Mach 3 jet to grow at a slower rate, and to exhibit stronger low-wavenumber components in the early stages of its development than the Mach 2 jet.

3. Simulation results

3.1. *Flow development*

3.1.1. *Vorticity field*

Instantaneous fields of the vorticity norm are represented in figure 3 for the two jets at times $t = 5r_0/u_j$, $t_c - 10r_0/u_j$, t_c and $t_c + 10r_0/u_j$, where t_c is the time of the potential core closure. This time, defined as the time when the mean centreline velocity reaches the value of $0.95u_j$, is equal to $25.3r_0/u_j$ for the jet at $M_j = 2$ and to $61.1r_0/u_j$ for the jet at $M_j = 3$. At $t = 5r_0/u_j$, the vorticity is concentrated in thin axisymmetric mixing layers separating the inner potential core of the jet and the ambient medium. Very slight perturbations are distinguishable in the mixing layers and correspond to the instability waves growing from the initial excitation. At $t = t_c - 10r_0/u_j$, the mixing layers are thicker than previously, due to the development of turbulent structures. The mixing layers of the Mach 3 jet exhibit larger scales than those of the Mach 2 jet, which is consistent with the linear stability analysis predicting that the most amplified axial wavenumber is lower at a higher Mach number. At $t = t_c$, the mixing layers from the opposite sides of the jet begin to interact on the centreline. Finally, the jets are fully mixed at $t_c + 10r_0/u_j$.

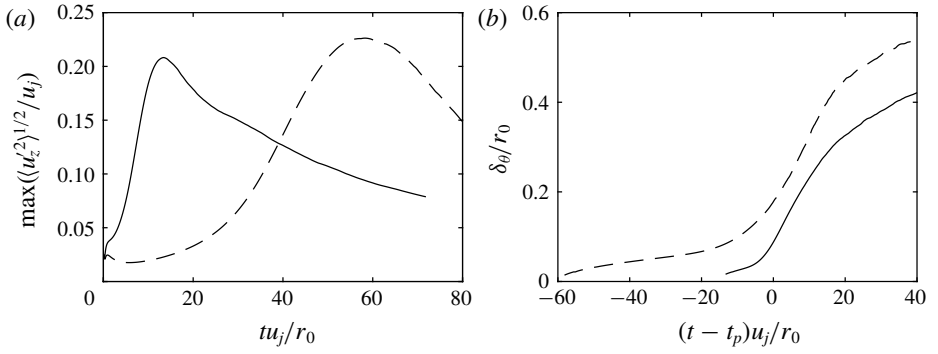

FIGURE 4. Time variations of (*a*) maximum r.m.s. value of axial velocity fluctuations and (*b*) shear-layer momentum thickness for —— $M_j = 2$ and - - - - $M_j = 3$.

3.1.2. *Mean and fluctuating axial velocity fields*

The time variations of the maximum root-mean-square (r.m.s.) values of axial velocity fluctuations are presented in figure 4(*a*). For the two jets, the velocity fluctuations start at $t = 0$ at a value close to 2 % of the jet velocity and then rise and reach a peak at a time $t_p = 13.4r_0/u_j$ for $M_j = 2$ and $t_p = 58.2r_0/u_j$ for $M_j = 3$. The peak value is approximately equal to 20 % of the jet initial velocity and can be attributed (Bogey & Bailly 2010) to the pairing of vortices when the jet shear layers transition from a laminar to a turbulent state. This time t_p will be used as a reference throughout the paper to perform comparison between the two jets. It is longer for the Mach 3 jet than for the Mach 2 jet, which can be explained by the lower growth rate of instability waves in the former case.

The shear-layer momentum thicknesses are represented in figure 4(*b*) as a function of $t - t_p$. Initially, it grows slowly as the shear layers are in a laminar state. At $t \simeq t_p$, as the jets transition from a laminar to a turbulent state, the momentum thickness rapidly increases and grows at a fast pace until the closing of the potential core, when the mixing layers join and merge on the jet axis. Then, the momentum thickness continues to grow, but at a slower rate.

3.1.3. *Spectra of velocity fluctuations*

The power spectral densities of the axial velocity fluctuations at $r = r_0$ at $t = 5r_0/u_j$, $t_p - 10r_0/u_j$, t_p and $t_p + 10r_0/u_j$ are represented in figure 5 as a function of the axial wavenumber. The grid cutoff wavenumber $k_z r_0 = 62.8$ is also displayed. At $t = 5r_0/u_j$, as the jet mixing layers are still in a laminar state, the spectra obtained for the two jets display a distinctive hump close to the most unstable wavenumber predicted from linear stability analysis, i.e. for $k_z r_0 = 5.2$ at $M_j = 2$ and for $k_z r_0 = 3$ at $M_j = 3$. In appendix A, this peak wavenumber is shown not to depend on the strength of the initial forcing. At $t = t_p$, when the jets transition to a turbulent state, the spectra are broadband thanks to the presence of turbulent fluctuations in the jet shear layers. At subsequent times, for $t = t_p + 10r_0/u_j$ and $t_p + 20r_0/u_j$, the spectra display a similar shape to that at $t = t_p$. Moreover, at $t = t_p + 20r_0/u_j$, the spectral slopes are close to the $k_z^{-5/3}$ slope characteristic of turbulence at equilibrium over a little less than one wavenumber decade. Further later, at $t = t_p + 55r_0/u_j$ for instance, the spectra, not shown for brevity, display a wider inertial range because of the fully developed state of the turbulence at these times.

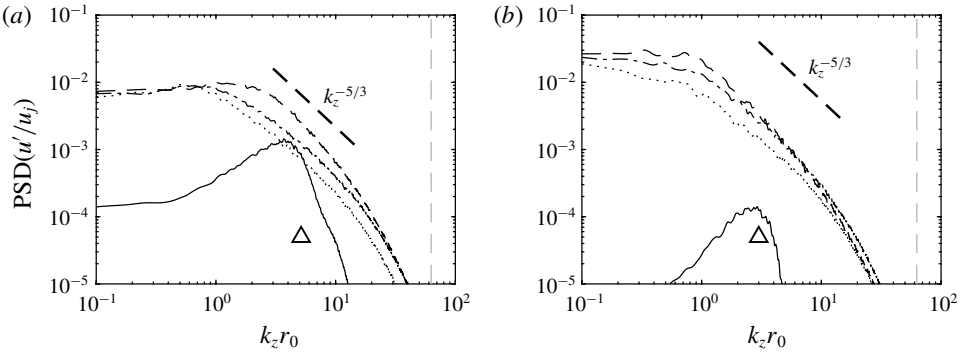

FIGURE 5. Representation, for (*a*) $M_j = 2$ and (*b*) $M_j = 3$, of the power spectral densities of axial velocity fluctuations at $r = r_0$ normalised by u_j as a function of the axial wavenumber at times —— $5r_0/u_j$, - - - - t_p, — · — $t_p + 10r_0/u_j$ and · · · · · · $t_p + 20r_0/u_j$. The triangle indicates the most amplified wavenumber at $t = 0$ and the dashed grey line indicates the grid cutoff wavenumber.

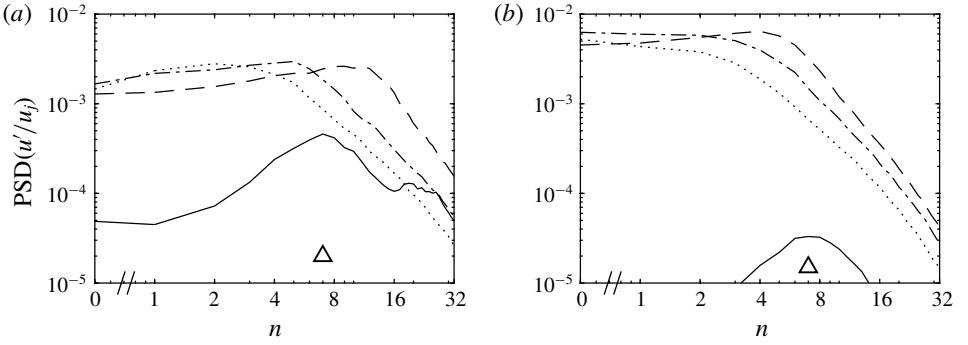

FIGURE 6. Representation, for (*a*) $M_j = 2$ and (*b*) $M_j = 3$, of the power spectral densities of axial velocity fluctuations at $r = r_0$ normalised by u_j as a function of the azimuthal mode number at times —— $5r_0/u_j$, - - - - t_p, — · — $t_p + 10r_0/u_j$ and · · · · · · $t_p + 20r_0/u_j$. The triangle indicates the most amplified mode number at $t = 0$.

The azimuthal power spectral densities of axial velocity fluctuations computed at $r = r_0$ are shown in figure 6 as a function of the azimuthal mode number n at the same times as the spectra in figure 5. At $t = 5r_0/u_j$, the most energetic mode is the seventh azimuthal mode, which is also the most amplified one based on the linear stability analysis. At later times, the spectra are broader, following the jet transition from a laminar to a turbulent state, which causes the formation of turbulent fluctuations over a wide range of mode numbers. The peak mode number also decreases over time, as visible in the spectra at $t = t_p + 10r_0/u_j$ and $t_p + 20r_0/u_j$.

3.2. *Near pressure field*

3.2.1. *Statistical properties of the near pressure field*

The time variations of the r.m.s. value of pressure fluctuations at $r = 8r_0$ are plotted in figure 7(*a*). For the two jets, a peak is reached at $t \simeq t_p + 12r_0/a_\infty$, due to the generation of intense acoustic waves during the development of the jets. The peak

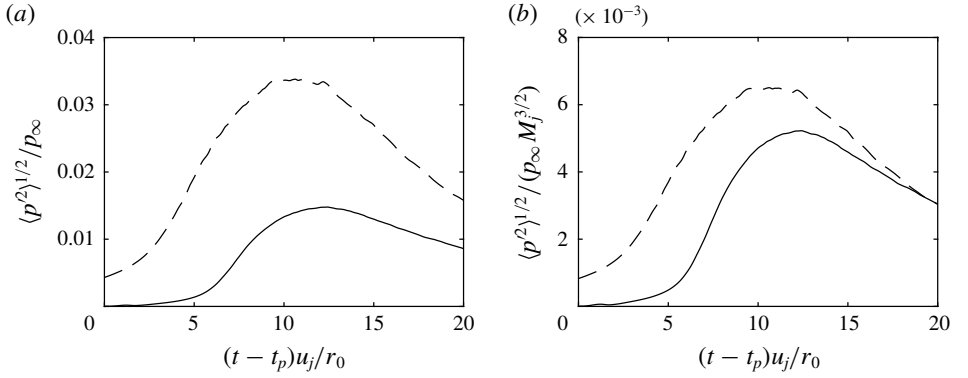

FIGURE 7. Time variations of the r.m.s. value of pressure fluctuations at $r = 8r_0$ normalised by (*a*) p_∞ and (*b*) $p_\infty M_j^{3/2}$ for —— $M_j = 2$ and - - - - $M_j = 3$.

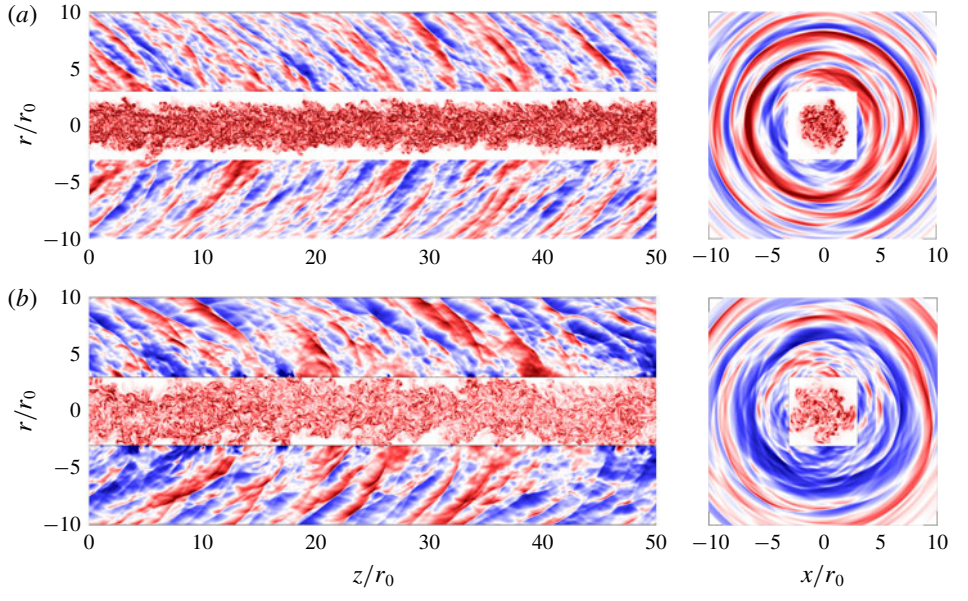

FIGURE 8. (Colour online) Snapshots of pressure fluctuations and vorticity norm at $t = t_p + 12r_0/a_\infty$ for (*a*) $M_j = 2$ and (*b*) $M_j = 3$. The colour scales range from $-0.02p_\infty M_j^{3/2}$ to $0.02p_\infty M_j^{3/2}$ for the pressure and up to $3u_j/r_0$ for the vorticity, from blue to red.

pressure is stronger for the Mach 3 jet than for the Mach 2 jet, as expected, which is due to the higher speed of the former. In addition, when normalised by $M_j^{3/2}$, the peak pressure levels do not significantly differ in figure 7(*b*), which is consistent with a common assumption that the sound intensity produced by supersonic jets varies with the third power of the jet speed (Ffowcs Williams 1963). After the peak, the pressure fluctuations gradually weaken over time, following the decrease of the velocity fluctuation intensity.

Snapshots of the pressure fluctuations and vorticity fields in the (r, z) and (r, θ) planes are provided in figure 8 at the time $t_p + 12r_0/a_\infty$ of peak levels for $r = 8r_0$,

M_j	$S(p)$	$K(p)$	$S(\Theta)$	$K(\Theta)$
2	0.27	3.2	−2.6	16.8
3	0.40	3.7	−3.3	24.1

TABLE 1. Values at $r = 8r_0$ and $t = t_p + 12r_0/a_\infty$ of the normalised skewness S and kurtosis K of the pressure p and dilatation Θ.

as well as in the corresponding movies movie_figure8a and movie_figure8b available online at https://doi.org/10.1017/jfm.2019.729 for $M_j = 2$ and $M_j = 3$, respectively. In the (r, z) plane, straight, elongated wavefronts propagating in the downstream direction are observed in the vicinity of the flow. They are very similar to the Mach waves observed in simulations (de Cacqueray *et al.* 2011; Nichols *et al.* 2013*b*), as well as in optical visualisations (Lowson & Ollerhead 1968; Kearney-Fischer, Kim & Samimy 2011; Murray & Lyons 2016) for spatially developing supersonic jets. In addition, the snapshots in the (r, θ) plane reveal organised wavefronts spanning the entire circumference of the jets, highlighting the strong azimuthal correlation of the sound field. Some of the waves in the snapshots of figure 8 have an asperous, jagged aspect, especially in the case of the Mach 3 jet, which indicates the presence of shock-like, steepened waves. As in the study of Nichols *et al.* (2013*a*), these fast compression waves are visible in the immediate vicinity of the jet flow and appear to be associated with the coherent, elongated Mach waves that dominate the sound field. They also appear to be significantly correlated in the azimuthal direction, which will be investigated into further details later on in the paper.

In the past, several statistical indicators have been proposed in order to quantify the presence of such steepened waves (Ffowcs Williams 1963; McInerny 1997; Krothapalli, Arakeri & Greska 2003; Falco 2007; Baars & Tinney 2014). Notably, the skewness and kurtosis factors provide useful information on the asymmetry and intermittency of the sound field (Ffowcs Williams *et al.* 1975; Mora *et al.* 2014; Fiévet *et al.* 2016). Their values, computed at $r = 8r_0$ and at $t = t_p + 12r_0/a_\infty$ for the pressure and dilatation fields, are reported in table 1. For both jets, the skewness and kurtosis factors of the pressure fluctuations are significantly higher than the values 0 and 3 expected for a Gaussian distribution, as observed in jets emitting crackle noise. In addition, the skewness factor of the dilatation is negative, while its kurtosis factor takes large, positive values, revealing the intermittent presence of strong, shock-like compressions in the signals. As expected, the present indicators are stronger, in absolute value, at Mach 3 than at Mach 2, which shows that the waves generated by the jets are steeper, more positively skewed and more intermittent at the highest Mach number.

In order to explore the structure of the sound field from a more quantitative perspective, axial and azimuthal power spectral densities of pressure fluctuations obtained at $r = 8r_0$ at $t = t_p + 12r_0/a_\infty$ are shown in figure 9. They are normalised by $p_\infty M_j^3$, following the assumption that sound intensity varies with the third power of the jet speed. In figure 9(*a*), the spectra are plotted as a function of $k_z\delta_\theta(t_p)$, where $\delta_\theta(t_p)$ is the shear-layer momentum thickness at time t_p, and is equal to $0.09r_0$ for $M_j = 2$, and to $= 0.18r_0$ for $M_j = 3$. This choice is motivated by the expectation that the dominant wavelength in the pressure field should scale according to the shear-layer thickness at time of peak noise emission, arbitrarily estimated as $t = t_p$. The reasonably good collapse of the spectra confirms this assumption. In particular, they both peak

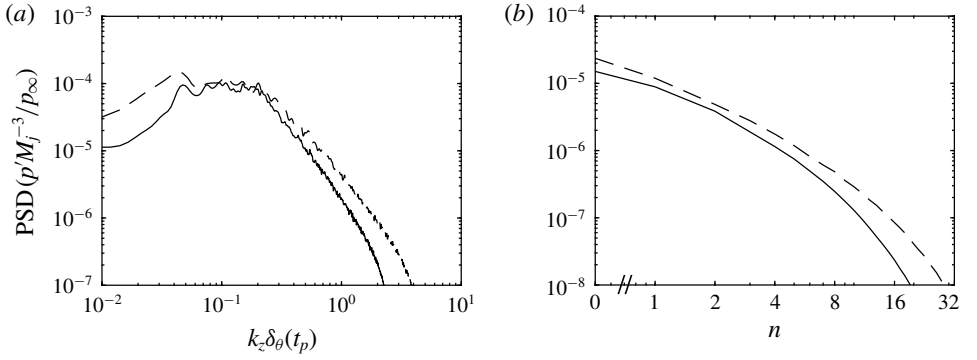

FIGURE 9. Pressure fluctuation spectra at $t = t_p + 12r_0/a_\infty$ normalised by $p_\infty M_j^3$ as a function of (*a*) axial wavenumber and (*b*) azimuthal mode number for —— $M_j = 2$ and ---- $M_j = 3$.

for a wavenumber $k_z\delta_\theta(t_p) \simeq 0.2$, yielding acoustic wavelengths of approximately $2.8r_0$ for $M_j = 2$ and $5.7r_0$ for $M_j = 3$. The collapse is however less obvious at low and high wavenumbers, where the pressure levels are higher for $M_j = 3$ than for $M_j = 2$. In the high-wavenumber range, this excess is due to the presence of more shock-like structures in the jet near field, as indicated by the skewness and kurtosis factors in table 1. Indeed, the sharp compressions associated with these structures are expected to cause an increase of the energy contained in high-wavenumber components. In the low-wavenumber range, the discrepancy is likely to be due to the presence of low-frequency, hydrodynamic components whose spectra are not expected to scale according to M_j^3 (Arndt, Long & Glauser 1997).

The pressure power spectral densities are also plotted as a function of the azimuthal mode number in figure 9(*b*). In all cases, the dominant azimuthal mode number is the axisymmetric one, and the energy decay is rapid at higher mode numbers. In particular, 87 % of the total sound intensity radiated by the Mach 2 jet is contained within the azimuthal modes of order 0 to 4 whereas 82 % of the total intensity is contained within these modes for the Mach 3 jet. The results are in agreement with experimental (Troutt & McLaughlin 1982) and numerical (de Cacqueray *et al.* 2011; Sinha *et al.* 2014) studies of spatially developing supersonic jets, where low-order azimuthal modes are prevalent in the noise radiated in the downstream direction.

3.2.2. *Azimuthal structure of the steepened waves*

In order to illustrate the main features of the steepened waves radiated by the jets, the pressure fluctuations obtained at $r = 8r_0$ at $t = t_p + 12r_0/a_\infty$ are provided in figure 10. Two steepened, shock-like waves are clearly visible at $z = 223.6r_0$ and $z = 226r_0$. Their shapes are typical of the structures observed near jets radiating crackle noise. In particular, a rapid compression phase yields to a strong positive pressure peak and it is followed by a gradual expansion having a much wider extent than the initial compression, spanning approximately over $2r_0$. The pressure profiles reconstructed from all of the Nth first azimuthal modes, with N ranging from 0 to 4 are also plotted in figure 10. Rapid compressions are not found in the waveforms obtained for $N = 0$, when only the axisymmetric mode is considered. Rather, the compressions associated with the shocks are progressively unveilled as more modes are included in the reconstruction of the pressure field. In particular, for $N = 4$,

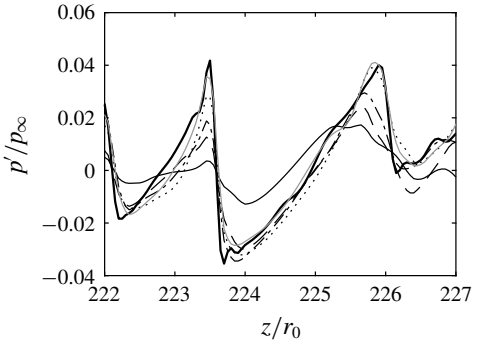

FIGURE 10. Profiles of pressure fluctuations at $r = 8r_0$ at $t = t_p + 12r_0/a_\infty$ for $M_j = 2$; partial sum of the azimuthal modes from mode 0 to mode N, with —— $N=0$, - - - - $N=1$, — · — $N=2$, · · · · · · $N=3$ and —— (grey) $N=4$ and —— full signal.

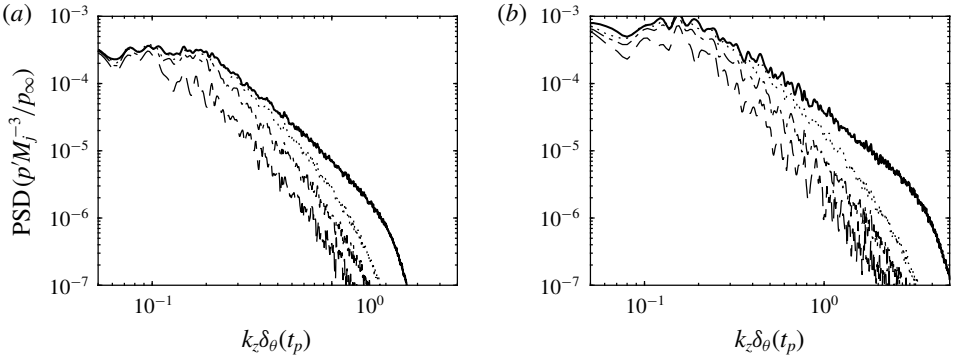

FIGURE 11. Pressure fluctuation spectra at $r = 8r_0$ at $t = t_p + 12r_0/a_\infty$ for (*a*) $M_j = 2$ and (*b*) $M_j = 3$; partial sum of the azimuthal modes from mode 0 to mode N, with - - - - $N=0$, — · — $N=1$ and · · · · · · $N=4$ and —— full signal.

all of the most important features of the full field are present, including the sharp compression waves.

The power spectral densities of the signals reconstructed from the Nth first azimuthal modes are plotted for $N=0$, 1 and 4 in figure 11, as a function of the axial wavenumber. For the two jets, the spectra for $N=0$ closely match those for the full fields at very low wavenumbers but significantly differ for $k_z r_0 \geqslant 0.1$. For instance, for $M_j = 2$, the axisymmetric mode contains more than 95 % of the total sound intensity for $k_z\delta_\theta = 0.1$, but only 10 % for $k_z\delta_\theta = 0.5$. The agreement between the reconstructed and full pressure fields is satisfactory over a wider range of wavenumbers as more modes are included in the reconstruction. For $N = 4$, the spectra obtained for the reconstructed field closely match those for the full field up to $k_z\delta_\theta(t_p) \simeq 0.6$ although significant differences persist in the high-wavenumber range, for $k_z\delta_\theta(t_p) \geqslant 1$ for instance. However, based on the analysis of the waveforms in figure 10, the missing, high-wavenumber components associated with modes higher than 4 are not expected to significantly change the structure of steepened waves, whose most peculiar features are associated with low-order modes. For that reason, the following study of their generation process is limited to the azimuthal reconstruction of the flow and sound

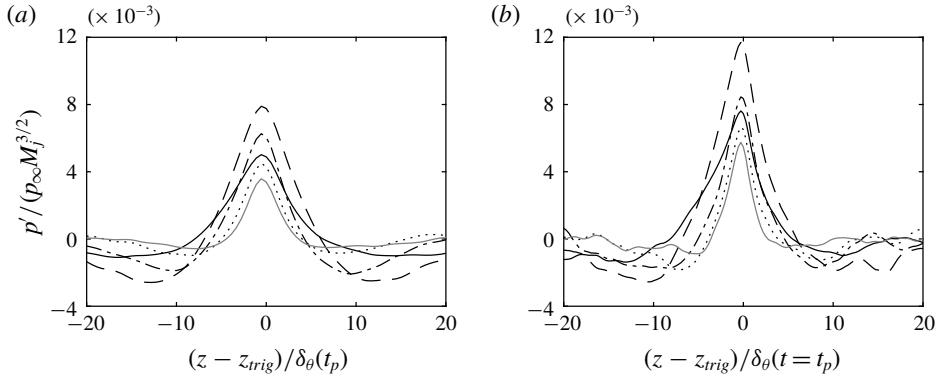

FIGURE 12. Axial profiles of the conditionally averaged pressure at $t = t_{trig}$ and $r = r_{trig}$ for (*a*) $M_j = 2$ and (*b*) $M_j = 3$; azimuthal modes —— $n = 0$, - - - - $n = 1$, — · — $n = 2$, · · · · · · $n = 3$ and —— (grey) $n = 4$.

fields with $N = 4$. This should facilitate the analysis by filtering out the contribution of these high-order azimuthal modes.

3.3. *Mechanisms at the origin of the steepened waves*

3.3.1. *Conditional averages of the wave generation process*

In order to investigate the mechanisms leading to the generation of steepened waves, a conditional averaging procedure is applied to the flow and sound fields of the jets. This technique consists in synchronising several flow events over a detection criterion, before performing an ensemble average such that only recurrent, generic features remain (Antonia 1981). When the trigger condition is related to the acoustic pressure field, conditional averages constitute a powerful tool for the study of sound generation mechanisms since they allow flow events associated with noise production to be described (Mercier, Castelain & Bailly 2018; Bogey 2019; Schmidt & Schmid 2019). In the present study, the conditional averages are triggered by the detection of extreme maxima of pressure fluctuations at a distance $r_{trig} = 4.5r_0$ from the jet axis, in the very near acoustic field. This location has been empirically chosen to be far enough from the flow that acoustic disturbances are dominant in the pressure field but close enough that nonlinear propagation effects have only a weak impact on the acoustic waves. The profiles of pressure fluctuations obtained at time $t_{trig} = t_p + 6r_0/a_\infty$, close to the time of peak pressure levels at $r = r_{trig}$, are binned in intervals of length $30\delta_\theta(t_p)$ in the axial direction, corresponding to an axial wavenumber $k_z\delta_\theta(t_p) \simeq 0.2$, close to the peak of the spectra in figure 9. For each interval, the pressure maximum is determined, and the flow and sound fields are synchronised according to the axial and azimuthal coordinates of peak pressure, labelled z_{trig} and θ_{trig}, and ensemble averaged.

The conditional averaging procedure is first applied to individual azimuthal modes of the pressure field, as in the study of Schmidt & Schmid (2019). For the two jets, the axial variations of the waveforms obtained at $t = t_{trig}$ and $r = r_{trig}$ are shown in figure 12 for the first five azimuthal modes. The signals are normalised by $M_j^{3/2}$ and plotted as a function of $(z - z_{trig})/\delta_\theta(t_p)$, using the same length scale reference as for the spectra in figure 9. For the two jets, and for all mode numbers, the conditionally

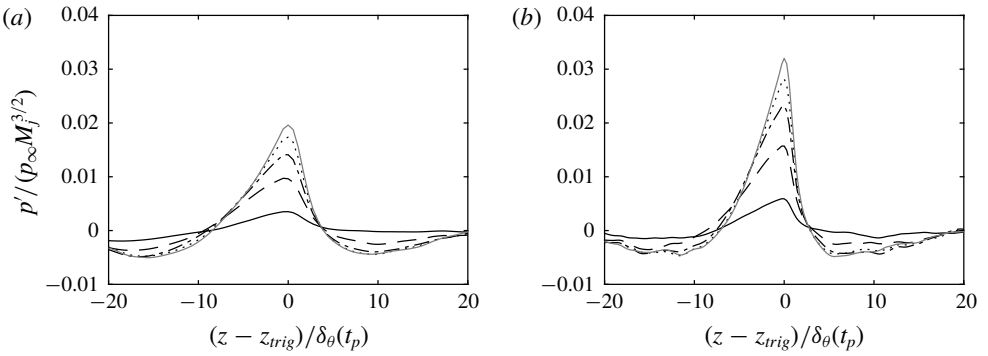

FIGURE 13. Axial profiles of the conditionally averaged pressure in the plane $\theta = \theta_{trig}$ at $t = t_{trig}$ and $r = r_{trig}$ for (*a*) $M_j = 2$ and (*b*) $M_j = 3$; partial sum up to order N with —— $N = 0$, - - - - $N = 1$, — · — $N = 2$, · · · · · · $N = 3$ and —— (grey) $N = 4$.

averaged pressure fluctuations are maximum for $z = z_{trig}$, as expected given the synchronisation condition. Moreover, they remain positive over a distance which shortens with the mode number, and equal to approximately ten times the shear-layer momentum thickness. It is noteworthy that none of the waveforms exhibits sharp compressions such as those in the signals reconstructed from the first five modes in figure 10. Instead, the conditional pressure fluctuations obtained for all mode numbers are symmetric with respect to the trigger position z_{trig}. This shows that steepened waves are not associated with one particular azimuthal mode of the pressure field, and suggests that several modes need to be superposed in order to recover their specific features.

On the basis of the above finding, the conditional averaging procedure is now applied to the pressure field reconstructed from all of the azimuthal modes of order ranging from $n = 0$ to 4. They are computed from 142 and 110 shock events for the jets at Mach 2 and 3, respectively, and this number is shown in appendix B to be sufficient to obtain converged statistics. The axial variations of the conditional waveforms at r_{trig} and t_{trig} are provided in figure 13 for the two Mach numbers, using the same normalisation as in figure 12. The partial sum of the azimuthal modes up to the order N is also represented for $0 \leqslant N \leqslant 4$, in order to highlight the contribution of the different modes. The steepened, asymmetric shape of the waveforms is clearly visible in the present conditional averages, and it is more pronounced as more azimuthal modes are included. Notably, the sharp compression and smooth expansion are observed for $N = 4$, confirming that only five modes are sufficient to recover the main features of the steepened shock-like waves. The peak of the conditional pressure does not scale according to the third power of the jet velocity, as the normalised pressure maximum is equal to 0.02 for $M_j = 2$ and to 0.03 for $M_j = 3$. This suggests that the conditional averages are computed from more extreme events at $M_j = 3$ than at $M_j = 2$, which is consistent with the higher skewness and kurtosis obtained for the former Mach number.

The azimuthal structure of the waves is illustrated in figure 14, where the conditional waveforms reconstructed from $N = 4$ for the jet at $M_j = 2$ are represented in the planes $\theta = \theta_{trig}$, $\theta_{trig} + \pi/6$, $\theta_{trig} + \pi/3$ and $\theta_{trig} + \pi/2$. As expected, the pressure is strongest in the detection plane at θ_{trig}, but rapidly decreases with increasing azimuthal angle, so that the levels obtained for $\theta = \theta_{trig} + \pi/2$ are more than ten

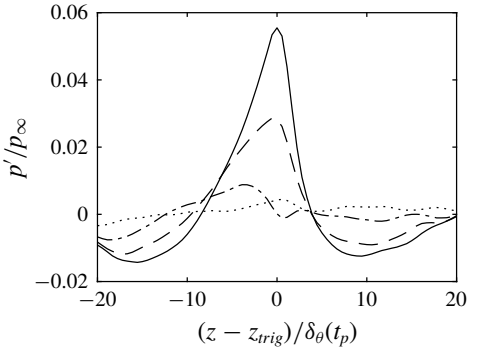

FIGURE 14. Conditionally averaged pressure at $r = r_{trig}$ and $t = t_{trig}$ for $M_j = 2$ represented in the plane —— $\theta = \theta_{trig}$, - - - - $\theta_{trig} + \pi/6$, — · — $\theta_{trig} + \pi/3$ and · · · · · · $\theta_{trig} + \pi/2$.

times lower than the maximum pressure. The waveforms are also smoother at a higher azimuthal angle, which indicates that the sharp compressions associated with the waves are localised over a narrow azimuthal extent centred around the detection angle θ_{trig}.

Conditional averages in the detection plane $\theta = \theta_{trig}$ are also computed at times $t < t_{trig}$ to provide a chronological description of the events leading to the formation of the steepened waves. Two-dimensional plane views of the conditional pressure and radial velocity fields are shown in figure 15 at times $t = t_p + 1.5r_0/a_\infty$, $t_p + 3r_0/a_\infty$, $t_p + 4.5r_0/a_\infty$ and $t_p + 6r_0/a_\infty$; see also the corresponding movies movie_fig15a and movie_fig15b. The sonic line, defined as $u_z = a_\infty$, is also represented to highlight the upper limit of the jet supersonic core. The conditional flow and sound fields obtained for the two Mach numbers are very similar. At $t_p + 1.5r_0/a_\infty$, a straight, inclined pressure wave emerges from the jet, upstream of $z = z_{trig}$. It consists of a positive peak surrounded by two bands of negative levels, and its shape reminds us that of wavepacket disturbances extracted from simulations of spatial supersonic jets by Sinha *et al.* (2014), for instance. Inside the jet flow, the inner tip of this pressure disturbance is directly connected to a large-scale perturbation of the radial velocity, located in the inner, supersonic core of the jet. A slight indentation of the sonic line is associated with this disturbance. At $t_p + 3r_0/a_\infty$, the inner tip of the wave remains connected to the velocity disturbance, which is still located in the supersonic side of the jet, but downstream from its initial position. Finally, for $t_p + 4.5r_0/a_\infty$ and $t_p + 6r_0/a_\infty$, the wave separates from the flow and propagates in the downstream direction.

The inclination angle α_{cond} of the waves can be estimated from the orientation of the pressure gradient, computed at the location of minimum dilatation. At time t_{trig}, this yields $\alpha_{cond} = 46°$ for $M_j = 2$ and 53° for $M_j = 3$. Thus, the acoustic waves radiated by the jet at $M_j = 3$ are more inclined than at $M_j = 2$, which can be related to the higher convection speed in the latter case. This speed can be estimated from the relation

$$u_c = \frac{a_\infty}{\cos \alpha_{cond}}, \tag{3.1}$$

leading to $u_c = 1.5a_\infty$ for $M_j = 2$ and $1.7a_\infty$, for $M_j = 3$. These values can be compared with those obtained from the axial position of the minimum of radial velocity in the lower, high-speed part of the jet. This position, shown in figure 16 varies approximately linearly, indicating a nearly constant convection speed, close

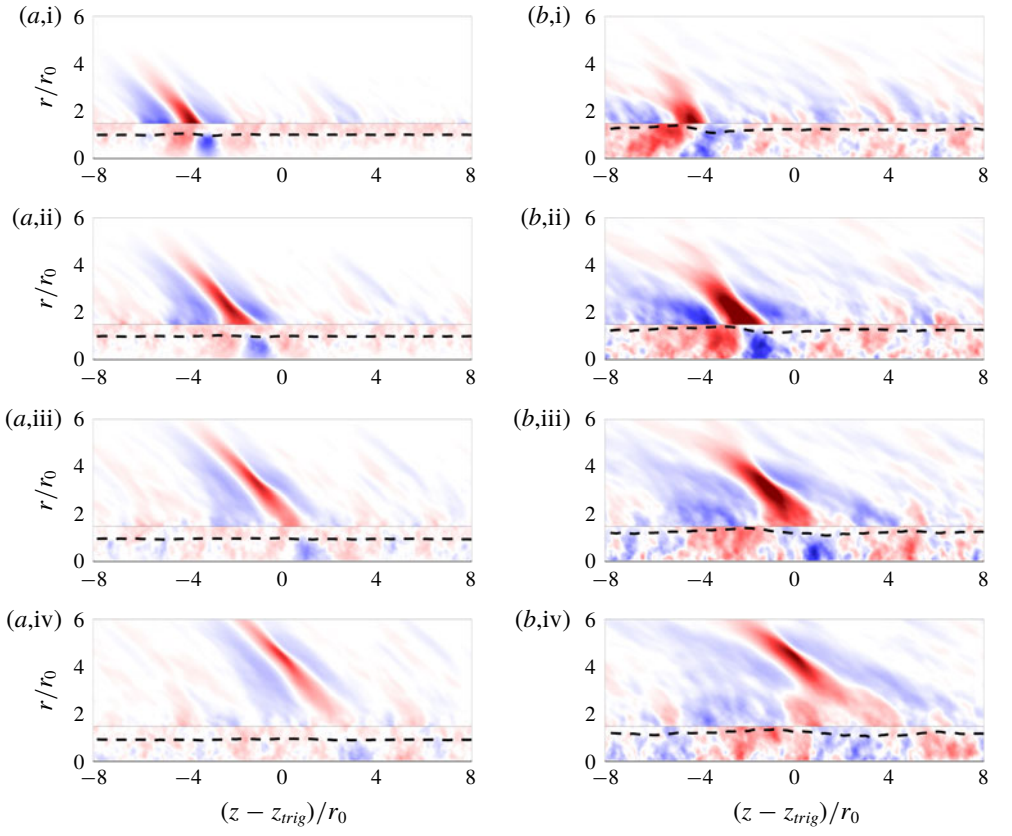

FIGURE 15. (Colour online) Conditionally averaged pressure and radial velocity fluctuations for (*a*) $M_j = 2$ and (*b*) $M_j = 3$ at times (i) $t_p + 1.5r_0/a_\infty$, (ii) $t_p + 3r_0/a_\infty$, (iii) $t_p + 4.5r_0/a_\infty$ and (iv) $t_p + 6r_0/a_\infty$. The dashed line indicates the sonic line and the colour scales range from $-0.03p_\infty M_j^{3/2}$ to $0.03p_\infty M_j^{3/2}$ for the pressure and up to $0.1u_j$ for the radial velocity, from blue to red.

to $u_c = 0.7u_j = 1.4a_\infty$ for $M_j = 2$ and to $0.55u_j = 1.65a_\infty$ for $M_j = 3$, which are in good agreement with those estimated from the wavefront inclinations. This strongly suggests that the waves in the conditional averages are Mach waves produced by the flow large-scale coherent structures. This is further supported by the variations of the location of peak conditional pressure, also represented in figure 16. This location is indeed very similar to that of the minimum of radial velocity from t_p to $t_p + 3r_0/a_\infty$, i.e. when the pressure wave is attached to the flow disturbance. This is not true for $t \geqslant t_p + 4r_0/a_\infty$, when the wave separates from the flow disturbance and propagates away from the jet. During that time, the position of the peak pressure still increases linearly, but at a speed close to the value of $a_\infty \cos\alpha_{cond}$ obtained assuming a propagation in the direction predicted from (3.1).

The present conditional averages thus show a direct link between the formation of steepened waves and the supersonic convection of large-scale flow disturbances located inside the jets. These flow disturbances have supersonic convection speeds, persist over significant length and time scales, and bear some resemblance to large-scale coherent structures extracted in jets at lower speed (Yule 1978; Bogey 2019). This provides

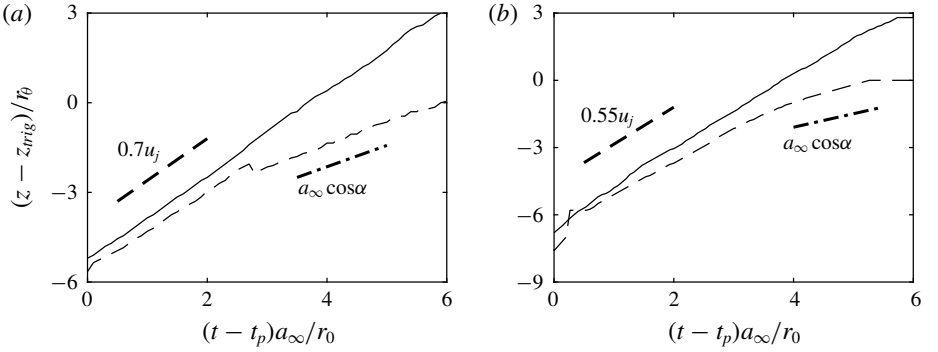

FIGURE 16. Time evolution of the axial positions of —— minimum radial velocity and ---- maximum pressure in the plane at $\theta = \theta_{trig}$ for (*a*) $M_j = 2$ and (*b*) $M_j = 3$.

evidence that steepened waves generated by supersonic jets are a particular, nonlinear case of Mach wave radiations by coherent structures, as proposed in previous studies (Nichols *et al.* 2013*a*; Murray & Lyons 2016; Buchta & Freund 2017). Given their nonlinear nature, steepened waves only appear when several azimuthal modes are simultaneously considered and thus cannot be related to one particular, azimuthal mode.

3.3.2. *Flow events at the origin of the steepened waves*

The connection between the steepened waves and the flow disturbances is further explored in order to determine what particular aspect of the flow structures causes Mach waves to steepen near the source. To this end, the conditional averaged fields constitute a useful tool since they provide an idealised, generic view of the coherent structures connected with the waves. The conditionally averaged pressure field obtained for the jet at $M_j = 2$ is displayed in figure 17 at $t_p + 2r_0/a_\infty$, close to the time when the steepened waves are generated; see also the corresponding movie available online at journals.cambridge.org/flm/figure17. The flow field is also represented as a vector field showing the direction and magnitude of the conditionally averaged velocity fluctuations. At the lower tip of the wave, a vortical structure associated with a pressure deficit is visible below the sonic line and can be interpreted as the trace of coherent structures in the shear layers. Upstream of this structure, a stagnation point with a pressure excess is also found past the coherent vortex. When convected by the jet flow, this velocity perturbation acts upon the surrounding medium as a wavy wall travelling at a supersonic speed (Ribner 1969). In most models of Mach wave radiation (Tam & Burton 1984*b*; Sinha *et al.* 2014), it is assumed that the relation between the flow disturbance and the Mach wave is linear, and shock formation is thus prohibited. However, this linear assumption will not hold if the flow perturbation is strong enough. In such a case, nonlinear effects could result in the formation of steepened, positively skewed Mach waves as observed, for instance, by Buchta & Freund (2019) who solved the nonlinear Euler equations for a supersonic flow over a wavy wall.

Determining at what point a flow perturbation is strong enough for wave steepening to occur is not straightforward. Indeed, there is no obvious way to define a strength parameter for flow perturbations such as the ones revealed in the conditional averages,

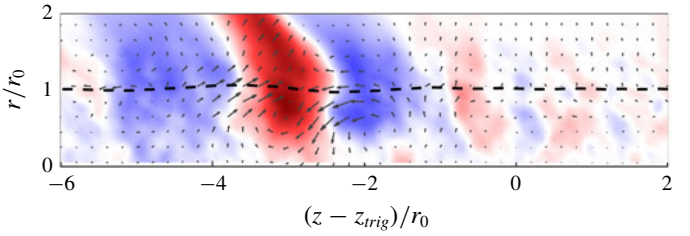

FIGURE 17. (Colour online) Conditionally averaged pressure and velocity at $t = t_p + 2r_0/a_\infty$ for $M_j = 2$. The pressure fluctuations are represented in colour, the arrows represent the velocity fluctuations and the dashed line indicates the sonic line. The colour scale for the pressure ranges from $-0.1p_\infty$ to $0.1p_\infty$, from blue to red.

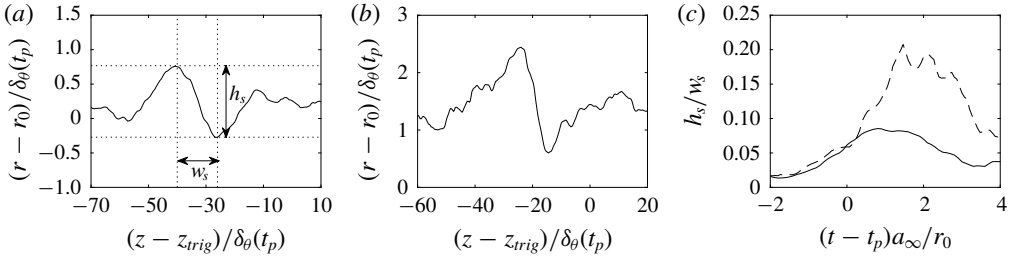

FIGURE 18. Radial position of the sonic line at $t = t_p + 2r_0/a_\infty$ for (*a*) $M_j = 2$ and (*b*) $M_j = 3$ and (*c*) time variations of the aspect ratio h_s/w_s of the sonic-line disturbance for —— $M_j = 2$ and - - - - $M_j = 3$.

which are more complex than a wavy wall. One possibility is to consider the displacement of the sonic line induced by the large-scale vortex. This is motivated by the fact that the sonic line is close to the location $r = r_0$ of maximum Reynolds stress, so that the amplitude of its displacement is related to that of the velocity fluctuations induced by the coherent structures. Moreover, since the sonic line delimitates the flow region with supersonic speed with respect to the ambient medium, the flow perturbations below this line are expected to be efficient sound generators. The radial position of the sonic line is represented in figure 18(*a*,*b*) as a function of the axial coordinate for the two jets. In both cases, it has a wavy shape, and shows a peak and a trough located upstream and downstream from the pressure wave, respectively. The height h_s of the structure is defined as the difference between the extreme radial positions of the sonic line, whereas its width w_s is given by the difference between the locations of the peak and trough, as illustrated in figure 18(*a*).

The aspect ratio of the sonic-line disturbance, defined as h_s/w_s, is introduced as a strength parameter for the structures correlated with the waves. Indeed, following Tam & Hu (1989), the amplitude of the acoustic pressure wave produced by a sinusoidal wavy wall moving at a supersonic speed is proportional to the product ϵk_z, where ϵ and k_z are the amplitude and wavenumber of the wavy-wall disturbance, respectively. Thus, assuming for the present flow that the amplitude and axial wavenumber of the wavy wall are such that $\epsilon = h_s$ and $k_z = 2\pi/w_s$, coherent structures with a higher aspect ratio are expected to cause a stronger deviation of the surrounding flow, leading to

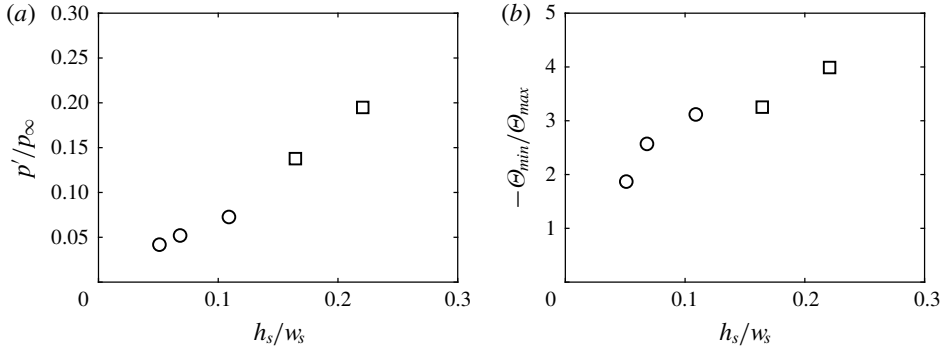

FIGURE 19. Representation of (a) the peak conditional pressure at $r = r_{trig}$ and (b) the steepness parameter $-\Theta_{min}/\Theta_{max}$ as a function of the aspect ratio of the sonic-line disturbance at $t = t_p + 2r_0/a_\infty$ for ○ $M_j = 2$ and □ $M_j = 3$.

the production of more intense and steeper Mach waves. The ratio h_s/w_s obtained for the two jets is plotted as a function of time in figure 18(c). It is close to 0 at $t = t_p - 2r_0/a_\infty$, and rapidly increases until it reaches a peak at $t \simeq t_p + 2r_0/a_\infty$, which is near the time when the pressure wave is generated. Moreover, the peak value is stronger for $M_j = 3$, than for $M_j = 2$, as it is equal to 0.2 and 0.1, respectively.

The relationship between the aspect ratio of the flow disturbances and the steepened waves is finally investigated. To this end, the detected pressure events are sorted for each jet according to the value of the positive pressure peak at $r = r_{trig}$ and $t = t_{trig}$ and split into different groups of equal size depending on the value of their pressure maxima. Three such groups are defined for the Mach 2 jet, so that the pressure peaks are compared against the first and second tercile of their distribution. For $M_j = 3$, only two groups are considered, so that the pressure peaks are compared with the median of the distribution. Indeed, fewer shock events are available in that case with respect to $M_j = 2$, due to the lower number of simulated runs. The number of groups is thus lower in order to maintain a number of events that is statistically significant.

The conditional averages are computed separately for the different groups following the same procedure as previously. In particular, the mean pressure maximum computed for all groups at $r = r_{trig}$ and $t = t_{trig}$ is plotted in figure 19(a) as a function of the aspect ratio of the sonic-line displacement, computed at $t = t_p + 2r_0/a_\infty$. A linear variation is obtained, showing a direct correlation between the strength of the pressure waves and the aspect ratio of the coherent structures which produce them. This relation is consistent with the assumption that the coherent structures extracted by the conditional averaging procedure produce sound by acting upon the surrounding medium as a supersonically moving wavy wall. This result also confirms that the aspect ratio of the structures, as defined from the sonic-line displacement, provides a simple yet relevant way to assess the tendency of flow structures to produce strong Mach waves.

The effects of the aspect ratio of the structures on the steepened aspect of the waves is finally assessed by considering a wave steepening parameter defined as $-\Theta_{min}/\Theta_{max}$, where Θ_{min} and Θ_{max} are the minimum and maximum of the conditional dilatation computed at $r = r_{trig}$ and $t = t_{trig}$. The steepening parameter is plotted in figure 19(b) as a function of the structure aspect ratios. It is higher than 1 in all cases, indicating that the compressions in the conditional averages are steeper than

the associated expansions. More importantly, the steepening parameter increases with the aspect ratio of the sonic-line disturbance, thus showing that Mach waves are not only stronger for higher values of this parameter, but that they are also steeper.

4. Conclusion

In the present paper, the azimuthal structure and generation process of steepened acoustic waves by supersonic axisymmetric shear flows are investigated by performing large eddy simulations of temporal round jets. Two isothermal jets at Mach numbers of 2 and 3 and at a diameter-based Reynolds numbers of 12 500 are simulated, and their initial development is validated against linear stability. In particular, the most amplified wavenumbers and azimuthal modes compare favourably with those predicted from temporal stability analysis. In addition, the Mach 3 jet spreads more slowly than the Mach 2 jet and contains stronger low-wavenumber components. After their transition from a laminar to a turbulent state, the two jets radiate intense Mach waves with a shock-like, steepened aspect, such as those observed near supersonic jets radiating crackle noise. This is reflected in the high values of the skewness and kurtosis factors of the pressure and dilatation computed close to the jets, which show a strong asymmetry and intermittency of the near field. As for spatially developing jets at similar Mach numbers, the sound fields of the jets are dominated by low-order azimuthal modes, which are investigated separately by reconstructing the pressure field from its first, low-order Fourier components. No steepened waves are observed in the axisymmetric mode, but steeper wavefronts progressively arise as more than one mode are involved. This is explained by the observation that low-wavenumber components in the pressure spectra are mostly associated with low-order mode numbers, whereas high-wavenumber components are essentially supported by high-order modes. Despite this, the shape of the steepened waves is clearly recovered when as low as five modes are considered, which highlights their strong azimuthal correlation.

The generation process of the waves is then investigated by applying a conditional averaging procedure. No steepened waves are present in the averages when the procedure is applied to only one azimuthal mode, highlighting their nonlinear nature. Therefore, the conditional averaging procedure is then applied to the pressure field reconstructed from all of the first five modes. In that case, the distinctive shape of the waves is recovered over a relatively narrow extent of the jet circumference. The conditional averages are also used to describe the generation process of steepened waves by synchronising and ensemble averaging the flow fields at times preceding the detection of the pressure peaks. These averages show a direct link between the formation of steepened waves and the supersonic motion of large-scale flow disturbances which are located in the inner, supersonic core of the jets and persist over significant length and time scales. When they are convected downstream by the jet, these structures act upon the surrounding medium as a supersonic wavy wall, causing the formation of intense Mach waves presenting a steepened aspect over a limited azimuthal portion of the jet circumference. Finally, the strength and steepness of the waves are directly related to the shape of the structures which generate them, and more particularly to their aspect ratio, defined as the ratio between their radial and axial extents. Indeed, the structures which extend deep into the jet flow, such as those in the shear layers of the Mach 2 jet, cause a stronger deviation of the surrounding flow field than structures which are elongated in the flow direction, thus leading to the formation of steeper Mach waves. This result is consistent with the observation that passive noise reduction devices such as chevron or nozzle inserts,

which alter the shape of the large-scale structures near the nozzle, can reduce the crackling behaviour of supersonic jets (Martens, Spyropoulos & Nagel 2011; Murray & Lyons 2016).

Acknowledgements

This work was granted access to the HPC resources of FLMSN (Fédération Lyonnaise de Modélisation et Sciences Numériques), partner of EQUIPEX EQUIP@MESO, and of the resources of IDRIS (Institut du Développement et des Ressources en Informatique Scientifique) under the allocation 2018-2a0204 made by GENCI (Grand Equipement National de Calcul Intensif). It was performed within the framework of the Labex CeLyA of Université de Lyon, operated by the French National Research Agency (grant no. ANR-10-LABX-0060/ANR-16-IDEX-0005). Finally, the authors gratefully acknowledge R. Sabatini for performing linear stability analyses from the jet flow profiles.

Supplementary movies

Supplementary movies are available at https://doi.org/10.1017/jfm.2019.729.

Appendix A. Influence of the initial excitation

In this first appendix, the influence of the amplitude of the initial excitation procedure on the early development of instability waves is examined. To this end, three simulations are carried out for the jet at $M_j = 2$ by considering different values for the amplitude α_{exc} of the initial excitation. The first simulation has $\alpha_{exc} = 0.04$, which is the value used for the simulations presented in the present paper. The amplitude of the excitation used in the two other simulations is lower with respect to the reference case, as $\alpha_{exc} = 0.01$ and 0.0025. The power spectral densities of the axial velocity fluctuations obtained at $r = r_0$ and $t = 5r_0/u_j$, in the early, laminar phase of the jet development, are represented in figure 20(*a*) as a function of the axial wavenumber, and in figure 20(*b*) as a function of the azimuthal mode number. As

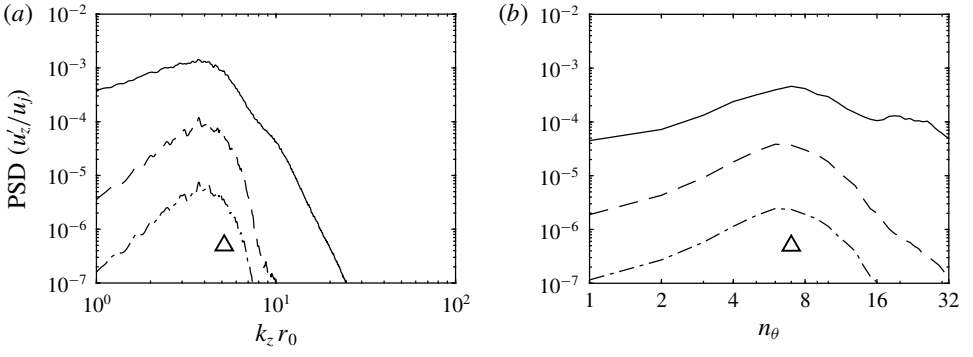

FIGURE 20. Power spectrum densities of the axial velocity fluctuations for the jet at $M_j = 2$ at $r = r_0$ and $t = 5r_0/u_j$ as a function of (*a*) the axial wavenumber and (*b*) the azimuthal mode number, and for three values of the excitation strength parameter α_{exc}: —— $\alpha_{exc} = 0.04$, - - - - $\alpha_{exc} = 0.01$ and — · — $\alpha_{exc} = 0.0025$. The triangles indicate the most amplified wavenumbers and mode numbers at $t = 0$.

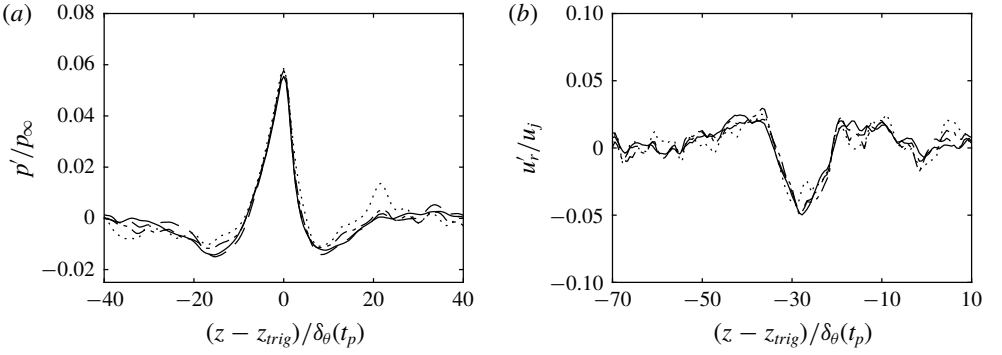

FIGURE 21. Representation for $M_j = 2$ of (a) the conditional pressure fluctuations at $r = 8r_0$ and $t = t_{trig}$ and (b) the radial velocity fluctuations at $r = 0.5r_0$ and $t = t_p + 2r_0/a_\infty$, computed using —— N_0, - - - - $N_0/2$, — · — $N_0/4$ and · · · · · · $N_0/8$ events.

expected, the spectra display higher levels for higher values of the initial excitation. Nevertheless, the spectra in figure 20(a) all share the same shape, with a distinctive hump centred around the wavenumber $k_z r_0 = 4$. This wavenumber does not seem to depend on the amplitude of the excitation, and is close to the value $k_z r_0 = 5.15$ predicted from the linear stability analysis of the initial profiles of § 2. Likewise, in figure 20(b), the azimuthal spectra obtained for the different amplitudes of the initial excitation also have a similar shape, with peak value reached for the mode $n = 7$ for $\alpha_{exc} = 0.04$, and $n = 6$ for $\alpha_{exc} = 0.01$ and 0.0025 which is also near the most amplified mode $n = 7$ estimated by the stability analysis. Thus, the initial development of the jets is consistent with the temporal linear analysis, regardless of the amplitude of the initial excitation.

Appendix B. Convergence of the conditional averages

The convergence of the conditional averages presented in § 3.3 is investigated for $M_j = 2$ by varying the number of events involved in their computations. To this end, the averages are computed using N_0, $N_0/2$, $N_0/4$ and $N_0/8$ events, where $N_0 = 142$ is the number of events used in § 3.3. The axial variations of the pressure fluctuations obtained at $r = 8r_0$ and $t = t_{trig}$ are plotted in figure 21(a). The signals obtained for $N_0/8$ events exhibit more noise than the others, suggesting that they are not fully converged. However, the averages computed for $N_0/4$ and $N_0/2$ do not significantly differ from those obtained from the full sample, indicating that using N_0 events is sufficient in order to obtain statistically converged pressure profiles. The conditional radial velocity fluctuations obtained at $r = 0.5r_0$ and $t = t_p + 2r_0/a_\infty$ are also plotted in figure 21(b) in order to show the convergence of the flow features correlated with the pressure events. The results are very similar when the number of events is greater than $N_0/4$. Thus, the number of events used in § 3.3 is sufficiently large to obtain converged conditionally averaged fields.

REFERENCES

ANTONIA, R. A. 1981 Conditional sampling in turbulence measurement. *Annu. Rev. Fluid Mech.* **13** (131), 131–156.

ARNDT, R. E. A., LONG, D. F. & GLAUSER, M. N. 1997 The proper orthogonal decomposition of pressure fluctuations surrounding a turbulent jet. *J. Fluid Mech.* **340**, 1–33.

BAARS, W. & TINNEY, C. E. 2014 Shock-structures in the acoustic field of a Mach 3 jet with crackle. *J. Sound Vib.* **333**, 2539–2553.

BAARS, W., TINNEY, C. E. & HAMILTON, M. F. 2014 On cumulative nonlinear acoustic waveform distorsions from high-speed jets. *J. Fluid Mech.* **749**, 331–366.

BAARS, W., TINNEY, C. E. & HAMILTON, M. F. 2016 Piecewise-spreading regime model for calculating effective Gol'dberg numbers for supersonic jet noise. *AIAA J.* **54** (9), 2833–2841.

BERLAND, C., BOGEY, C., MARSDEN, O. & BAILLY, C. 2007 High-order, low dispersive and low dissipative explicit schemes for multiple-scale and boundary problems. *J. Comput. Phys.* **224**, 637–662.

BOGEY, C. 2019 On noise generation in low Reynolds number temporal round jets at a Mach number of 0.9. *J. Fluid Mech.* **859**, 1022–1056.

BOGEY, C. & BAILLY, C. 2004 A family of low dispersive and low dissipative explicit schemes for noise computation. *J. Comput. Phys.* **194** (1), 194–214.

BOGEY, C. & BAILLY, C. 2006 Large eddy simulations of transitional round jets: influence of the Reynolds number on flow development and energy dissipation. *Phys. Fluids* **18**, 065101.

BOGEY, C. & BAILLY, C. 2010 Influence of nozzle-exit boundary-layer conditions on the flow and acoustic fields of initially laminar jets. *J. Fluid Mech.* **663**, 507–538.

BOGEY, C., BAILLY, C. & JUVÉ, C. 2003 Noise investigation of a high subsonic, moderate Reynolds number jet using a compressible LES. *Theor. Comput. Fluid Dyn.* **16** (4), 273–297.

BOGEY, C., DE CACQUERAY, N. & BAILLY, C. 2009 A shock-capturing methodology based on adaptative spatial filtering for high-order non-linear computations. *J. Comput. Phys.* **228**, 1447–1465.

BOGEY, C., MARSDEN, O. & BAILLY, C. 2011 Finite differences for coarse azimuthal discretization and for reduction of effective resolution near origin of cylindrical flow equations. *J. Comput. Phys.* **230**, 1134–1146.

BUCHTA, D. A. & FREUND, J. B. 2017 The near-field pressure radiated by planar high-speed free-shear-flow turbulence. *J. Fluid Mech.* **832**, 383–408.

BUCHTA, D. A. & FREUND, J. B. 2019 Intense sound radiation by high-speed flow: turbulence structure, gas properties, and near-field gas dynamics. *Phys. Rev. Fluids* **4**, 044605.

DE CACQUERAY, N. & BOGEY, C. 2014 Noise of an overexpanded Mach 3.3 jet: non-linear propagation effects and correlations with flow. *Intl J. Aeroacoust.* **13** (7–8), 607–632.

DE CACQUERAY, N., BOGEY, C. & BAILLY, C. 2011 Investigation of a high-Mach-number overexpanded jet using Large-Eddy simulation. *AIAA J.* **49** (10), 2171–2182.

CRIGHTON, D. G. & BASHFORTH, S. 1980 Nonlinear propagation of broadband jet noise. *AIAA paper* 1980-1039.

ENFLO, B. O. & HEDBERG, C. M. 2002 *Theory of Nonlinear Acoustics in Fluids*. Kluwer Academic Publisher.

FALCO, L. E. 2007 Single-point nonlinearity indicators for the propagation of high-amplitude acoustic signals. PhD thesis, Pennsylvania State University, PA.

FFOWCS WILLIAMS, J. E. 1963 The noise from turbulence convected at high speed. *Phil. Trans. R. Soc. Lond.* A **255** (1061), 469–503.

FFOWCS WILLIAMS, J. E., SIMSON, J. & VIRCHIS, V. J. 1975 'Crackle': an annoying component of jet noise. *J. Fluid Mech.* **71**, 251–271.

FIÉVET, R., TINNEY, C. E., BAARS, W. J. & HAMILTON, M. F. 2016 Coalescence in the sound field of a laboratory-scale supersonic jet. *AIAA J.* **54** (1), 254–265.

GALLAGHER, J. A. & MCLAUGHLIN, D. K. 1981 Experiments on the non linear propagation from low and moderate Reynolds number supersonic jets. *AIAA Paper* 1981-2041.

GEE, K. L., SPARROW, V. W., ATCHLEY, A. & GABRIELSON, T. B. 2007 On the perception of crackle in high-amplitude jet noise. *AIAA J.* **45** (3), 593–598.

GOJON, R. & BOGEY, C. 2017 Numerical study of the flow and the near acoustic fields of an underexpanded round free jet generating two screech tones. *Intl J. Aeroacoust.* **16** (7–8), 603–625.

HUSSAIN, A. K. M. F. 1983 Coherent structures: reality and myth. *Phys. Fluids* **26**, 2816–2850.

JORDAN, P. & COLONIUS, T. 2013 Wave packets and turbulent jet noise. *Annu. Rev. Fluid Mech.* **45**, 173–195.

KEARNEY-FISCHER, M., KIM, J. H. & SAMIMY, M. 2011 A study of Mach wave radiation using active control. *J. Fluid Mech.* **681**, 261–292.

KLEINMAN, R. R. & FREUND, J. B. 2008 The sound from mixing layers simulated with different ranges of turbulence scales. *Phys. Fluids* **20** (101503), 1–12.

KROTHAPALLI, A., ARAKERI, V. & GRESKA, B. 2003 Mach wave radiation: a review and an extension. *AIAA Paper* 2003-1200.

KROTHAPALLI, A., VENKATAKRISHNAN, L. & LOURENCO, L. 2000 Crackle: a dominant component of supersonic jet mixing noise. *AIAA Paper* 2000-2024.

LAUFER, J., SCHLINKER, R. & KAPLAN, R. E. 1976 Experiments on supersonic jet noise. *AIAA J.* **14** (4), 489–497.

LOWSON, M. V. & OLLERHEAD, J. B. 1968 Visualization of noise from cold supersonic jets. *J. Acoust. Soc. Am.* **44** (2), 624–630.

MARTENS, S., SPYROPOULOS, J. T. & NAGEL, Z. 2011 The effects of chevrons on crackle-engine and scale model results. *Proceedings of the ASME Turbo Expo, GT2011-46417*. ASME.

MCINERNY, S. A. 1997 Launch vehicle acoustics part 2: statistics of the time domain data. *J. Aircraft* **33** (3), 518–523.

MCLAUGHLIN, D. K., MORISSON, G. L. & TROUTT, T. R. 1975 Experiments on the instability waves in a supersonic jet and their acoustic radiation. *J. Fluid Mech.* **69** (1), 73–95.

MERCIER, B., CASTELAIN, T. & BAILLY, C. 2018 Experimental investigation of the turbulent density – far field sound correlations in compressible jets. *Intl J. Aeroacoust.* **17** (4–5), 521–540.

MOHSENI, K. & COLONIUS 2002 Numerical treatment of polar coordinate singularities. *J. Comput. Phys.* **157** (10), 3593–3600.

MORA, P., HEEB, N., KASTNER, J., GUTMARK, E. J. & KAILASANATH, K. 2014 Impact of heat on the pressure skewness and kurtosis in supersonic jets. *AIAA J.* **52** (4), 777–787.

MORFEY, C. L. & HOWELL, G. P. 1980 Nonlinear propagation of aircraft noise in the atmosphere. *AIAA J.* **19** (8), 986–992.

MURRAY, N. E. & LYONS, G. W. 2016 On the convection velocity of source events related to supersonic jet crackle. *J. Fluid Mech.* **793**, 477–503.

NICHOLS, J. W., LELE, S. K., HAM, F. E., MARTENS, S. & SPYROPOULOS, J. T. 2013*a* Crackle noise in heated supersonic jets. *Trans. ASME J. Engng Gas Turbines Power* **135** (5), 051202.

NICHOLS, J. W., LELE, S. K. & SPYROPOULOS, J. T. 2013*b* The source of crackle noise in heated supersonic jets. *AIAA Paper* 2013-2197.

PAPAMOSCHOU, D. 1995 Evidence of shocklets in a counterflow supersonic shear layer. *Phys. Fluids* **7**, 233–235.

PETITJEAN, B. & MCLAUGHLIN, D. K. 2003 Experiments on the nonlinear propagation of noise from supersonic jets. *AIAA Paper* 2003-3127.

PETITJEAN, B., VISWANATHAN, K. & MCLAUGHLIN, D. K. 2006 Acoustic pressure waveforms measured in high speed jet noise experiencing nonlinear propagation. *Intl J. Aeroacoust.* **5** (2), 193–215.

PINEAU, P. & BOGEY, C. 2018 Study of the generation of shock waves by high-speed jets using conditional averaging. *AIAA Paper* 2018-3305.

REICHMAN, B. O., GEE, K. L., NEILSEN, T. B., SWIFT, S. H., WALL, A. T., GALLAGHER, H. L., DOWNING, J. M. & JAMES, M. M. 2017 Acoustic shock formation in noise propagation during ground run-up operations of military aircraft *AIAA Paper* 2017-4043.

RIBNER, H. S. 1969 Eddy Mach wave noise from a simplified model of a supersonic mixing layer. *Tech. Rep.* UTIAS technical note no. 146.

ROSSMANN, T., MUNGAL, M. G. & HANSON, T. K. 2001 Evolution and growth of large-scale structures in high compressibility mixing layers. *J. Turbul.* **9** (3), 1–16.

SCHMIDT, O. T. & SCHMID, P. J. 2019 A conditional space-time POD formalism for intermittent and rare events: example of acoustic bursts in turbulent jets. *J. Fluid Mech.* **867**, R2.

SEINER, J. M., PONTON, M. K., JANSEN, B. J. & LAGEN, N. T. 1992 The effects ot temperature on supersonic jet noise emission. In *14th DGLR/AIAA Aeroacoustics Conference*. vol. 1, pp. 295–307. AIAA, (*AIAA Paper* 92-2046).

SINHA, A., RODRIGUEZ, D., BRÈS, G. & COLONIUS, T. 2014 Wavepacket models for supersonic jet noise. *J. Fluid Mech.* **742**, 71–95.

TAM, C. K. W. & BURTON, D. E. 1984*a* Sound generated by instability waves of supersonic flows. Part 1. Two-dimensional mixing layers. *J. Fluid Mech.* **138**, 249–271.

TAM, C. K. W. & BURTON, D. E. 1984*b* Sound generated by instability waves of supersonic flows. Part 2. Axisymmetric jets. *J. Fluid Mech.* **138**, 273–295.

TAM, C. K. W., CHEN, P. & SEINER, J. M. 1992 Relationship between instability waves and noise from high-speed jets. *AIAA J.* **30** (7), 1747–1752.

TAM, C. K. W. & DONG, Z. 1996 Radiation and outflow boundary conditions for direct computation of acoustic and flow disturbances in a nonuniform mean flow. *J. Comput. Acoust.* **4** (2), 175–201.

TAM, C. K. W. & HU, F. Q. 1989 On the three families of instability waves of high-speed jets. *J. Fluid Mech.* **201**, 447–483.

TAM, C. K. W. & MORRIS, P. J. 1980 The radiation of sound by the instability waves of a compressible plane turbulent shear layer. *J. Fluid Mech.* **98** (2), 349–381.

TROUTT, T. R. & MCLAUGHLIN, D. K. 1982 Experiments on the flow and acoustic properties of a moderate-Reynolds-number supersonic jet. *J. Fluid Mech.* **116**, 123–156.

YULE, A. J. 1978 Large-scale structures in the mixing layer of a round jet. *J. Fluid Mech.* **89** (3), 413–432.

ZAMAN, K. B. M. Q. 1985 Effect of initial condition on subsonic jet noise. *AIAA J.* **23** (9), 1370–1373.